J Mater Sci (2010) 45:6187–6199
DOI 10.1007/s10853-010-4712-0

Microstructure and texture development in single layered and heterolayered PZT thin films

Fransiska Cecilia Kartawidjaja · Anbusathaiah Varatharajan · Nagarajan Valanoor · John Wang

Received: 10 April 2010 / Accepted: 11 June 2010 / Published online: 25 June 2010
© Springer Science+Business Media, LLC 2010

Abstract Single-layered $Pb(Zr_{0.7}Ti_{0.3})O_3$ and $Pb(Zr_{0.3}Ti_{0.7})O_3$ thin films and heterolayered $Pb(Zr_{1-x}Ti_x)O_3$ thin films consisting of alternating $Pb(Zr_{0.7}Ti_{0.3})O_3$ and $Pb(Zr_{0.3}Ti_{0.7})O_3$ layers were studied for their microstructure and texture development. The texture in the single-layered PZT films is affected by the Zr/Ti ratio as they have different crystallization behavior depending on the Zr/Ti ratio. With increasing film thickness, the average grain size of $Pb(Zr_{1-x}Ti_x)O_3$ increases. An unusually large grain size of 1–3 μm together with a strong (001)/(100) preferred orientation were observed for the heterolayered $PZ_{70}T_{30}$, whereby $Pb(Zr_{0.7}Ti_{0.3})O_3$ was used as the seeding layer, for film as thin as 150 nm. The film microstructure is refined drastically when the stacking sequence is changed, i.e., when $Pb(Zr_{0.3}Ti_{0.7})O_3$ is employed as the seeding layer. Thermal treatment of the $PZ_{70}T_{30}$ seeding layer also plays an important function in the microstructure development of the heterolayered $PZ_{70}T_{30}$ film. The formation of the large-grained film is correlated to the lowered nucleation energy of crystallizing $Pb(Zr_{0.7}Ti_{0.3})O_3$ by the top $Pb(Zr_{0.3}Ti_{0.7})O_3$. The $Pb(Zr_{0.3}Ti_{0.7})O_3$ layer facilitated the nucleation and crystallization of the $Pb(Zr_{0.7}Ti_{0.3})O_3$ amorphous seeding layer, whereby the overall microstructure of the heterolayered thin film was dictated by the $Pb(Zr_{0.7}Ti_{0.3})O_3$ seeding layer leading to the growth of larger PZT grains.

F. C. Kartawidjaja · J. Wang (✉)
Department of Materials Science and Engineering, Faculty of Engineering, National University of Singapore, Singapore 117574, Singapore
e-mail: msewangj@nus.edu.sg

A. Varatharajan · N. Valanoor
School of Materials Science & Engineering, The University of New South Wales, Sydney, NSW 2052, Australia

Introduction

In recent years, there has been extensive investigation into ferroelectric thin films, whereby their microstructure and orientation are properly controlled to optimize their electrical behavior [1–5]. Indeed, a proper control in thin film texture and microstructure is very important, as they strongly influence the ferroelectric and dielectric properties, such as relative permittivity (ε), remanent polarization (P_r), coercive field (E_c), and fatigue endurance. For example, it has been reported that ferroelectric films with properly controlled large grains exhibit better electrical properties as compared to those of the small-grained films, due to the high mobility of domain walls movement in large-grained films [6, 7].

The processing parameters that affect the microstructure and texture of ferroelectrics films include the substrate materials [8–10], seeding layer [11–13], thermal processing conditions (e.g., temperature and heating rate) [2, 14–16], film thickness [14, 17], and the composition represented by the ratio of Zr to Ti for PZT [3, 18–20]. As PZT thin film is known to nucleate heterogeneously at the substrate/film interface, the texture of PZT film can be tailored by choosing an appropriate substrate material. For example, PZT thin films with (100), (110), and (111) orientations can be obtained using single-crystal STO of the same orientation [10]. Seeding layer has also been shown to play an important role in affecting the microstructure development of PZT films. Doi et al. [13] reported that the insertion of $(Ba_{0.5}Sr_{0.5})TiO_3$ or $PbTiO_3$ seeding layers gave rise to a reduction in grain size of PZT (53/47) film. For the film deposited on platinized silicon substrate, it has been reported that the very thin films (<100 nm) exhibited (100) preferred texture, while the relatively thick films demonstrated (111) preferred texture or random orientation

[14, 17]. It has been proposed that (100) texture is formed due to the energetically favored growth of (100) plane in PZT [1, 21]. However, several investigators showed that an oxidizing or reducing atmosphere during thermal treatment could affect the final texture of the thin film [22–24]. Under an oxidizing atmosphere, PbO(100) is formed and (100)-oriented PZT nucleates at the PbO(100) buffer layer due to the lattice matching. The (111)-oriented PZT nucleates on Pt_xPb buffer layer, which is formed when a reducing atmosphere is employed, due to the identical (111) lattice [23, 25, 26]. Thermal processing is another parameter in fabricating ferroelectric thin films with different microstructure and textures. For example, the PZT (52/48) thin film formed by pyrolysis at intermediate temperature followed by a thermal treatment at high temperature demonstrated a high degree of (100) texture with sub-micron-sized fine grains, while the PZT (52/48) thin film directly annealed at high temperature exhibited a strong (111) texture with fine grains [14, 15, 27]. It has been suggested that at the intermediate pyrolysis temperature, the formation process for PZT is rather slow, whereby the initially formed Pt_xPb undergoes decomposition to form PbO and becomes the seeding layer for PZT(100). The crystallization of amorphous PZT to perovskite structure is initiated by the formation of fluorite/pyrochlore structures, where both exhibit an fcc structure for cations and therefore are closely related to each other. However, the two phases are differentiated in the ordering of A^{2+} and B^{4+} cations, which is present in pyrochlore and absent in fluorite structure. The lattice parameter of pyrochlore is about twice that of fluorite [28, 29]. In this article, the term "fluorite" is used to refer to the intermediate PZT phase. The nucleation and growth of perovskite phase from the intermediate fluorite/pyrochlore phase may also be involved at different temperature stages, depending on the composition of PZT film. It has been reported that the transformation to perovskite phase in PZT is nucleation-dependent, due to the high activation energy of nucleation [30]. However, the activation energy for nucleation decreases with increasing Ti content in PZT composition. Therefore, rather different film textures and microstructures have been reported for different PZT compositions. The Zr-rich PZT films tend to lead to large perovskite grains, while Ti-rich films tend to give rise to small, submicron perovskite grain sizes [3, 18, 20, 31].

We have previously reported that heterolayered $PZ_{70}T_{30}$ films with (001)/(100) preferred orientation can be successfully deposited [32, 33]. These heterolayered thin films demonstrated unusually large grain sizes in the range of 1–3 μm, regardless of the film thickness. The large grains in the heterolayered film structure have demonstrated a further interesting phenomenon. As reported by Anbusathaiah et al. [34], a complex nanoscale ferroelastic-domain arrangement in the top $PZ_{30}T_{70}$ layer of bilayered heterostructure was observed by piezoresponse force microscopy (PFM) and cross-sectional transmission electron microscopy (TEM). These domains were susceptible to external field and led to a giant piezoelectric coefficient of 220 pm V^{-1}. Further observations with the single-layered $PZ_{70}T_{30}$ and $PZ_{30}T_{70}$ confirmed they did not have the same complex domain arrangement as the bilayered film; although, the single-layered $PZ_{70}T_{30}$ thin film was electroactive, whereby it was easily movable under external electric field.

On the basis of these previous understandings, the objective of this study is to investigate the formation and development of film texture and microstructure of heterolayered PZT. For comparison purposes, single-layered PZT film which consists of Zr-rich PZT ($Pb(Zr_{0.7}Ti_{0.3})O_3$) layer and Ti-rich PZT ($Pb(Zr_{0.3}Ti_{0.7})O_3$) layer are first studied for their phase transformation behavior, microstructure, and texture development. As discussed later, the information gained with these single-layered thin films provide useful insight into the texture and microstructure development of the heterolayered PZT thin films. The texture and microstructure development are studied by looking at both the structural and the processing parameters such as the stacking sequence, substrates, and the thermal treatment conditions. By comparing the effects of these parameters involved, the mechanisms behind the formation of unusually large grain and (001)/(100) preferred orientation in the heterolayered $PZ_{70}T_{30}$ is discussed.

Experimental section

The single-layered and heterolayered PZT thin films were prepared by a sol–gel process and deposited onto Pt(111)/$Ti/SiO_2/Si(100)$ substrate by spin coating. The thickness of the Pt layer is ~150 nm and that of Ti is ~50 nm. Two PZT precursor solutions, namely $Pb(Zr_{0.7}Ti_{0.3})O_3$ (coded as $PZ_{70}T_{30}$) and $Pb(Zr_{0.3}Ti_{0.7})O_3$ (coded as $PZ_{30}T_{70}$), were synthesized from $Zr[OCH(CH_3)_2]_4$, $Ti[OCH(CH_3)_2]_4$, and $Pb(CH_3COO)_2{\cdot}3H_2O$ as the starting materials. The single-layered and heterolayered PZT thin films were prepared by a sol–gel process and deposited onto $Pt/Ti/SiO_2/Si$ substrate by spin coating. The starting chemicals were dissolved in a mixture consisting of ethylene glycol monomethyl ether ($C_3H_8O_2$) and acetic acid (volume ratio = 5/1.3), where acetic acid acts as chelating agent to the metal alkoxides and reduces their sensitivity toward hydrolysis. The precursor solutions were 0.4 M in concentration with 10 mol% excess lead. For the single-layered PZT, the respective PZT precursor solution was spin-coated onto the platinized Si substrate, followed by drying at 300 °C for 5 min, baking at 500 °C for 7 min on

a hot plate, and then annealing at 650 °C for 1 h by RTA. The heterolayered PZT films were deposited by spin coating the $PZ_{70}T_{30}$ and $PZ_{30}T_{70}$ precursor solutions alternately. After each spin coating, the film was subjected to the same heat treatment as single-layered PZT film. After the required numbers of layer were obtained, the films were then annealed at 650 °C for 1.0 h by RTA. The heterolayered PZT thin film with $PZ_{70}T_{30}$ as the first layer is coded as heterolayered $PZ_{70}T_{30}$ thin film. Similarly, the heterolayered PZT thin film with $PZ_{30}T_{70}$ as the first layer is coded as heterolayered $PZ_{30}T_{70}$ thin film.

The phases present in and crystallinites of the films were characterized using X-ray diffractometer (Bruker AXS D8 Advanced, Karlsruhe, Germany) with a glancing/incident angle of 1.5°, which is a technique that is widely employed for characterization of thin films where the film thickness is smaller than the substrate thickness. SEM (Philips, XL 30, Hillsboro, OR) and AFM (Digital Instruments Multi-Mode Nanoscope III, Santa Barbara, CA) were employed to study the film morphologies and surface roughnesses. Raman (HORIBA Jobin–Yvon Labram HR800, Edison, NJ) measurements were performed at room temperature using 514.5 nm Argon laser as excitation source. The chemical states in the thin films were analyzed by X-ray photoelectron spectroscopy (Thermo Fisher Scientific Theta Probe A1333, Newington, NH). The elemental depth profiling of the heterolayered PZT thin films was also studied using secondary ion mass spectroscopy (ION-TOF-SIMS IV, Münster, Germany).

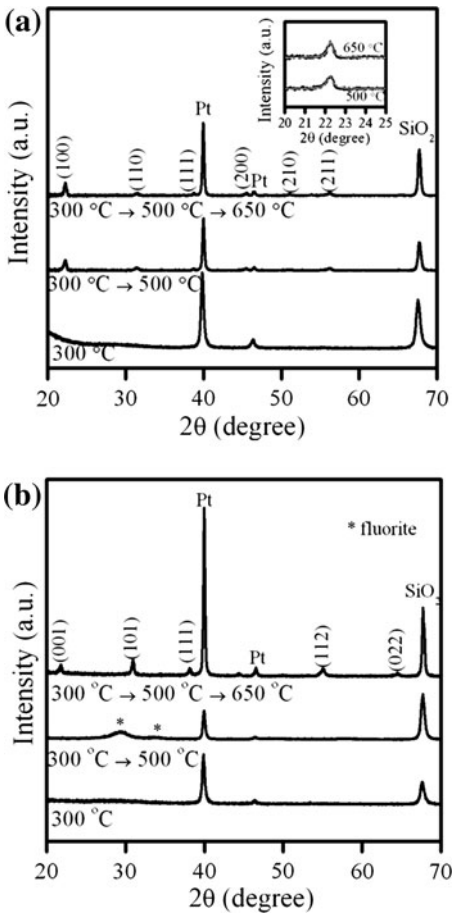

Fig. 1 XRD traces of the single-layered **a** $PZ_{30}T_{70}$ and **b** $PZ_{70}T_{30}$ thin films, treated with increasing temperature from 300° to 500° and finally to 650 °C as annealing temperature

Results and discussion

Single-layered PZT thin films

XRD phase analyses

The film texture and phases present in the single-layered PZT were investigated by XRD as shown in Fig. 1. Upon drying at 300 °C, both of the single-layered PZT films were largely in the amorphous phase form. With increasing annealing temperature, there is a phase transformation in the single-layered PZT, the temperature of which is dependent on the composition (Zr/Ti) ratio. The single-layered $PZ_{70}T_{30}$ formed fluorite phase as indicated by humps at 2θ of 29.5°, 33.5°, 49°, and 57.8° which correspond to (111), (200), (220), and (311) planes, respectively, after baking at 500 °C [35–37]. The fluorite structure was maintained even when the baking time was prolonged to 14 min as shown by the XRD traces in Fig. 2, demonstrating the stability of fluorite phase in $PZ_{70}T_{30}$. It was developed into a single perovskite phase when the annealing temperature was raised to 650 °C. The Ti-rich

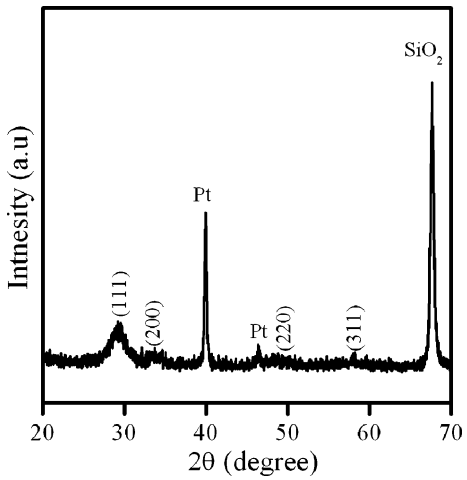

Fig. 2 XRD traces of the single-layered $PZ_{70}T_{30}$ thin film after baking for 14 min

single-layered $PZ_{30}T_{70}$ has a lower crystallization temperature as compared to that of the single-layered $PZ_{70}T_{30}$ film, whereby the perovksite structure can be steadily

Table 1 FWHM of (100) peaks and crystallite size calculations for single layered $PZ_{30}T_{70}$ thin films after thermal annealing at 500 and 650 °C

Temperature	500 °C	650 °C
FWHM (rad)	0.006431	0.005162
Crystallite size (nm)	21.7	27.1

formed after baking at 500 °C. The crystallinity of the $PZ_{30}T_{70}$ film increases with rising annealing temperature as shown by the increase in the intensities of XRD traces. The full-width at half maximum (FWHM) of XRD peak corresponding to (100), which is the strongest peak of the perovskite phase in the single-layered $PZ_{30}T_{70}$ film was analyzed. The crystallite sizes were calculated using the Debye–Scherer equation, as summarized in Table 1. It is observed that the peak width of (100) becomes narrower and sharper as the annealing temperature increases, showing that the crystallite size of the film increases. Crystallite sizes of 21.7 and 27.1 nm were calculated for the $PZ_{30}T_{70}$ film thermally annealed at 500 and 650 °C, respectively. For PZT thin films, the formation of crystalline perovskite phase from amorphous phase follows the sequences of: amorphous → fluorite/pyrochlore → perovskite. The Ti-rich PZT can form perovskite easily due to lower activation energy to nucleate the perovskite phase [3], while Zr-rich PZT form metastable fluorite/pyrochlore phase which then transforms to perovskite phase at higher temperature, since the stability of fluorite/pyrochlore phase is higher in Zr-rich PZT film [18].

A strong (100) preferred orientation is observed in the single-layered $PZ_{30}T_{70}$ film together with the formation of perovskite phase at 500 °C. As mentioned above, one of the plausible causes of the (100) preferred orientation in PZT films is due to the low interfacial energy of (100) making it the energetically favored growth plane [1, 21]. Another consideration was suggested by Chen and Chen [14], who studied the film pyrolized at an intermediate temperature such as 500 °C, the Pt_xPb interfacial layer that was formed readily could undergo oxidation and gave rise to an PbO(001) seeding layer for $PZ_{30}T_{70}$(100) to crystallize due to the similar lattice. Unlike the single-layered $PZ_{30}T_{70}$ film, upon annealing at 650 °C, perovskite phase was formed in the single-layered $PZ_{70}T_{30}$ film with random orientation similar to that in a ceramic bulk. The likely cause for this is due to the high volatility of PbO in $PZ_{70}T_{30}$ at high temperatures such that the nucleation at (100) is reduced and the nucleation occurred randomly with (101) as the highest peak. The high volatility of PbO in Zr-rich PZT that led to Pb-deficiency is also known to be responsible for the formation of the rosette structure in PZT [13, 38], which will also be discussed in "Film microstructure."

Raman studies

The Raman spectra of the single-layered PZT films are shown in Fig. 3. Typical Raman modes for rhombohedral and tetragonal structures are observed for single-layered $PZ_{70}T_{30}$ and $PZ_{30}T_{70}$ film, respectively. For $PZ_{70}T_{30}$, the rhombohedral phase with $C_{3v}^{5}(R3m)$ space group shows the Raman active modes of [39, 40]:

$$\Gamma_{\text{Raman-active}} = 3\text{A1} + 4\text{E}.$$

The Raman active modes for $PZ_{30}T_{70}$ in tetragonal structure with $C_{4v}^{1}(P4mm)$ space group are [39–41]:

$$\Gamma_{\text{Raman-active}} = 3\text{A1} + 4\text{E} + \text{B1}.$$

The Raman modes are assigned in accordance with the Raman studies of Burns and Scott [42] whose results are similar to those of other reports [39, 40]. The Raman peaks of the single-layered thin films were slightly shifted to lower frequencies when compared to those of the PZT in powder form [43]. It has been suggested that both the

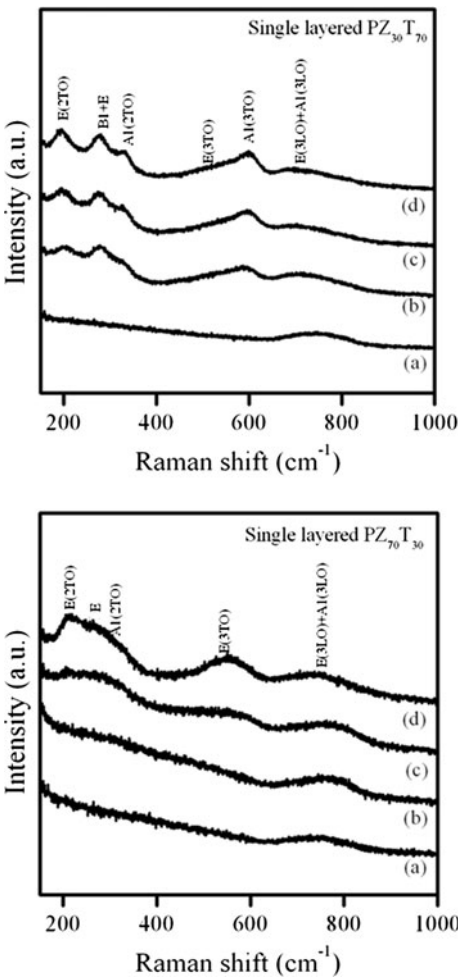

Fig. 3 Raman spectra of the single-layered $PZ_{30}T_{70}$ and $PZ_{70}T_{30}$ as a function of thermal treatment. (*a*) 300 °C, (*b*) 300 → 500 °C, (*c*) 300 → 580 °C, (*d*) 300 → 500 → 650 °C

crystallite size and the residual stresses in the films play an important role in affecting the positions of Raman peaks [44]. In an agreement with the XRD studies, the single-layered $PZ_{70}T_{30}$ film shows an amorphous structure after drying at 300 °C, as a broad shoulder is observed at 746 nm. With increasing temperature, the Raman spectra gradually changed and after annealing at 650 °C, the five Raman modes attributed to the rhombohedral structure were developed. Similarly, the Raman spectra for single-layered $PZ_{30}T_{70}$ show that with increasing temperature from 300 to 650 °C the amorphous phase was gradually transformed to tetragonal perovskite phase. The Raman modes were observed upon heating at 500 °C indicating that it crystallized at a lower temperature than $PZ_{70}T_{30}$ film, in an agreement with the XRD studies. With increasing temperature, the intensities of the Raman peaks increases showing an increase in film crystallinity (Fig. 4).

Comparing between single-layered $PZ_{70}T_{30}$ and $PZ_{30}T_{70}$ after annealing at 650 °C, the Raman peaks of $PZ_{70}T_{30}$ were broader and had lower intensities than those of $PZ_{30}T_{70}$, showing damping effect with increasing Zr/Ti ratio. It is also observed that the three Raman modes, namely E(2TO), B1 + E, and A1(2TO) formed a broad phonon band. Similar observation has been reported by Meng et al. [41].

Film microstructure

From the AFM images shown in Fig. 5a–f, it is observed that after baking, single-layered $PZ_{30}T_{70}$ film exhibited well-defined and homogenous nanograins, while the single-layered $PZ_{70}T_{30}$ film did not demonstrate well-defined grains. This is corresponding to the XRD traces discussed above, where the single-layered $PZ_{30}T_{70}$ film layer showed

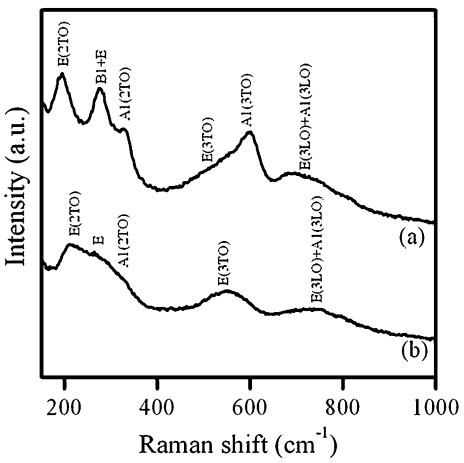

Fig. 4 Raman spectra of the single-layered (*a*) $PZ_{30}T_{70}$ and (*b*) $PZ_{70}T_{30}$ films after annealing at 650 °C

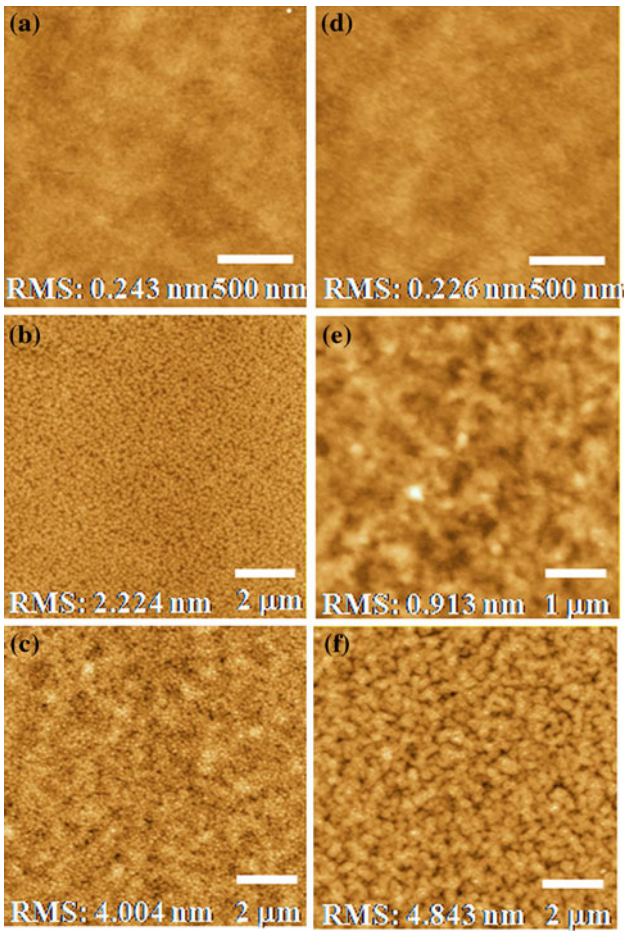

Fig. 5 AFM images of the single layered **a–c** $PZ_{30}T_{70}$ and **d–f** $PZ_{70}T_{30}$ after thermal treatment at **a**, **d** 300 °C, **b**, **e** 300 → 500 °C, **c**, **f** 300 → 500 → 650 °C

fully crystallized perovskite phase and the single-layered $PZ_{70}T_{30}$ film was a fluorite at 500 °C. Upon thermal annealing at 650 °C, the single-layered $PZ_{30}T_{70}$ film showed densely packed grains due to grain growth as shown in Fig. 5c with roughness of 4.004 nm, which was much lower than that of single-layered $PZ_{70}T_{30}$ film. The latter had crystallized into perovskite and formed nano-grains as shown in Fig. 5f, with a surface roughness of 4.843 nm. By increasing the film thickness from ~75 to ~450 nm, it is observed that the grain size increases, as shown in Fig. 6a–f. This is consistent with what has been reported by Park et al. [45], who observed that the grain size increases with increasing PZT film thickness. The composition dependence of PZT film microstructure is observed in this study, especially in thicker films. For single-layered $PZ_{30}T_{70}$, the grain size increased from an average of (119 ± 31.7) nm to (138.1 ± 21.3) nm together with a decreasing film roughness to 2.307. A much significant increase in grain size is observed for $PZ_{70}T_{30}$ film, together with an increasing film roughness to 13.237 nm as

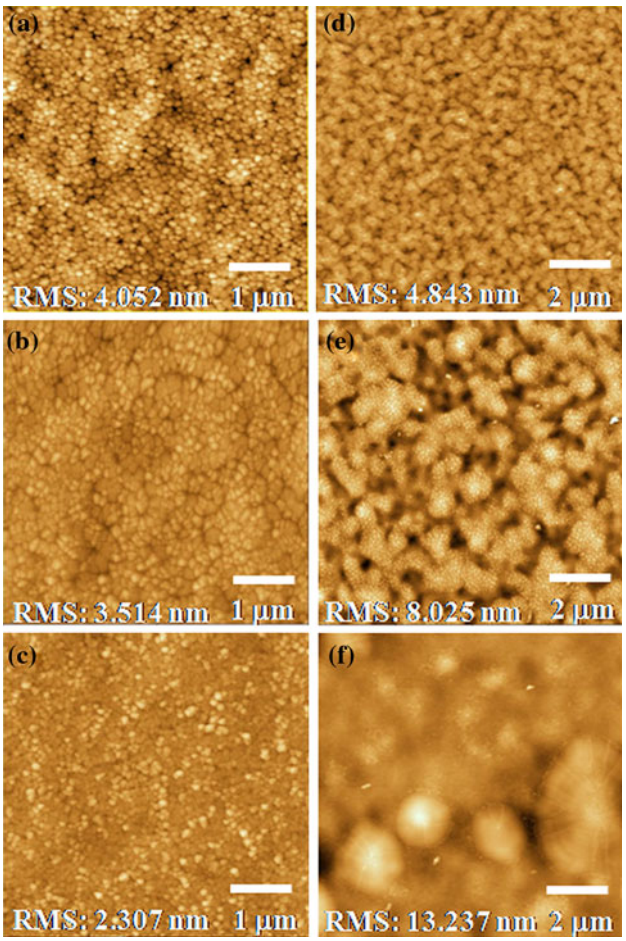

Fig. 6 AFM images of **a–c** $PZ_{30}T_{70}$ and **d–f** $PZ_{70}T_{30}$ films of different number of layers **a**, **d** single layer, **b**, **e** two layers, and **c**, **f** six layers after thermal annealing at 650 °C

the film thickness increases. The grain size was increased from (87.3 ± 22.9) nm to 1–2 μm. However, the thicker film was identified with rosette structure. The increase in roughness of $PZ_{70}T_{30}$ was due to the formation of the rosette structure in association with the volatility of Pb in PZT. The PZT film with Ti-rich composition showed a smaller grain size than that of the PZT film with Zr-rich composition. According to Kwok et al. [3], the low nucleation energy of $PZ_{30}T_{70}$ enables a high density of nuclei to form at lower temperature and the grain size is largely determined by the spacing between nuclei. The high nucleation energy of $PZ_{70}T_{30}$ in contrast enables fewer nuclei to form, where the nuclei can grow into much larger grains.

XPS studies

Figure 7 shows the XPS survey spectra for single-layered $PZ_{70}T_{30}$ and $PZ_{30}T_{70}$ films, respectively, after annealing at 650 °C. The high-resolution scan spectra of Pb 4*f*, Zr 3*d*, Ti

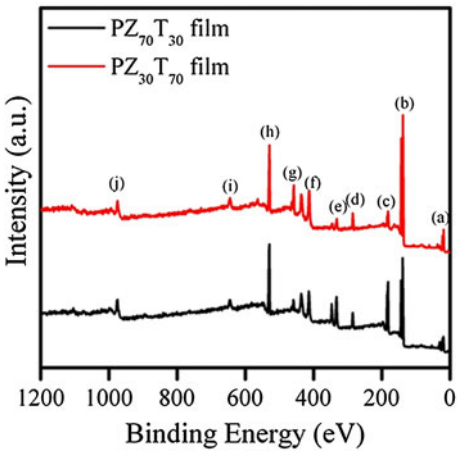

Fig. 7 The XPS survey spectra of the single-layered $PZ_{30}T_{70}$ and $PZ_{70}T_{30}$ films: (*a*) O 2*s*, (*b*) Pb 4*f*, (*c*) Zr 3*d*, (*d*) C 1*s*, (*e*) Zr 3*p*, (*f*) Pb 4*d*, (*g*) Ti 2*p*, (*h*) O 1*s*, (*i*) Pb 4*p*3, (*j*) O (Auger)

2*p*, and O 1*s* from both the films are shown in Fig. 8. The binding energies were corrected by taking C 1*s* signal at 285.0 eV as a reference. An individual element has only one spin–orbit doublet indicating that each element is in one chemical state. After the correction, the binding energy of Pb $4f_{7/2}$, Zr $3d_{5/2}$, and Ti $2p_{3/2}$ for $PZ_{70}T_{30}$ and $PZ_{30}T_{70}$ films are located at 137.8, 181.4, 458.1 eV, respectively. These are in agreement with previous reports, which indicate that the Pb, Zr, and Ti are in the Pb^{2+}, Zr^{4+}, and Ti^{4+} states [46–48]. The O 1*s* spectra can be decomposed into two peaks, the first peak of which is located at 529.6 eV corresponding to the binding energy of lattice oxygen in PZT. The second peak is located at 530.8 and 531.2 eV for $PZ_{30}T_{70}$ and $PZ_{70}T_{30}$, respectively, which is the binding energy of adsorbed oxygen at the surface [48]. There are no significant differences in XPS spectra between $PZ_{70}T_{30}$ and $PZ_{30}T_{70}$ films, in terms of the binding energy. In terms of intensity, the Pb peaks for $PZ_{70}T_{30}$ are lower indicating that there is higher degree of volatility of Pb in $PZ_{70}T_{30}$ film.

Heterolayered PZT thin films

Effect of seeding layers

XRD phase analyses Figure 9 shows the XRD traces of heterolayered PZT, after thermal baking at 500 °C and annealing at 650 °C. Upon baking at 500 °C, both films have been crystallized forming perovskite structure. While $PZ_{30}T_{70}$ 2-heterolayer has crystallized with no detectable fluorite phase, the $PZ_{70}T_{30}$ 2-heterolayer still shows a fluorite phase as indicated by the hump at 2θ of 29.5°. With further annealing at 650 °C, the film crystallinity was enhanced and both the film samples showed crystallized perovskite phase with (001)/(100) preferred orientation.

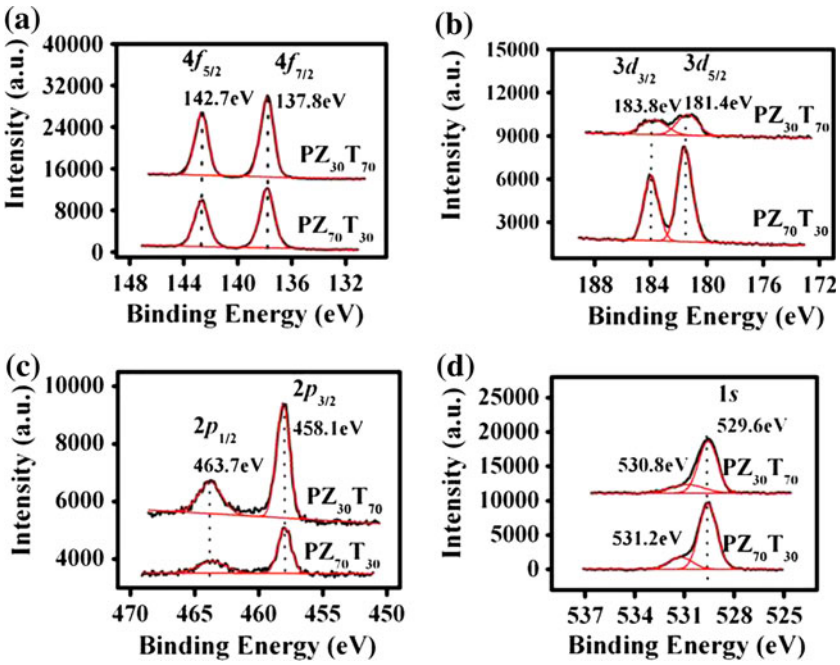

Fig. 8 The high-resolution scan spectra of **a** Pb 4*f*, **b** Zr 3*d*, **c** Ti 2*p*, and **d** O 1*s* of the single-layered $PZ_{30}T_{70}$ and $PZ_{70}T_{30}$ films

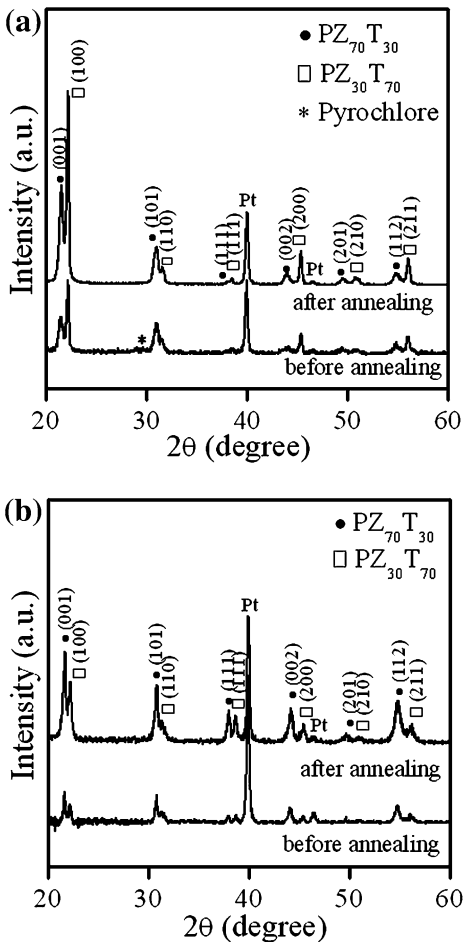

Fig. 9 XRD spectra of **a** $PZ_{70}T_{30}$ 2-heterolayer and **b** $PZ_{30}T_{70}$ 2-heterolayer before and after annealing at 650 °C

The stacking sequence of layer deposition causes little texture change in the heterolayered films.

SIMS The SIMS profiles of heterolayered PZT films are shown in Fig. 10, whereby the $PZ_{70}T_{30}$ layer is indicated by the region with higher Zr intensity and $PZ_{30}T_{70}$ layer is indicated by the region with higher Ti intensity. The profiles confirm the individual PZT layer is retained whereby a boundary is established between the alternating $PZ_{70}T_{30}$ and $PZ_{30}T_{70}$ layers. There was a degree of inter-diffusion at the interface between the first and the second layers of the heterolayered films, which is due to the surface roughness effect. The interface was well established with the increasing number of layers in the heterolayered film as the subsequent layer exhibited a smoother interface as we have previously reported [6].

Film microstructure and dielectric properties A large grain size in the range of 1–3 μm was observed for $PZ_{70}T_{30}$ 2-heterolayer as shown in Fig. 11a and b. Although coarse-grained PZT film of 1.5–3 μm has been reported in previous studies, they are normally formed in relatively thick films, >300 nm to 2.4 μm in thickness [3, 45]. The coarse-grained structure is often accompanied by the presence of cracks, which degrade the electrical behavior of PZT thin films. In the case of the heterolayered thin film, the large grains could be obtained in the film as thin as 150 nm, and they could be retained up to 450 nm in thickness for $PZ_{70}T_{30}$ 6-heterolayer with no crack formed [6]. Furthermore, the large grains in the heterolayered $PZ_{70}T_{30}$ thin film appear smooth with no occurrence of rosette structure,

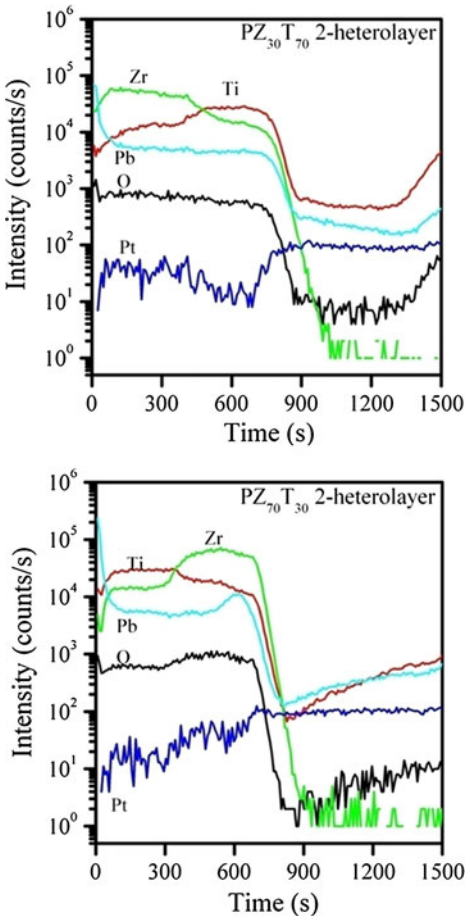

Fig. 10 SIMS depth profiling of $PZ_{30}T_{70}$ 2-heterolayer and $PZ_{70}T_{30}$ 2-heterolayer

which was observed for six-layered $PZ_{70}T_{30}$ film shown in Fig. 5f. Hence, by forming the heterolayered structure, the volatility of Pb especially from Zr-rich $PZ_{70}T_{30}$ layer can be suppressed and the rosette formation can be avoided. Interestingly, for the $PZ_{30}T_{70}$ 2-heterolayer, very fine grains were observed as shown in Fig. 11c and d, which is very different from the heterolayered $PZ_{70}T_{30}$ film. Increasing the film thickness to 450 nm, the $PZ_{30}T_{70}$ 6-heterolayer retained the small grain size which is similar to $PZ_{30}T_{70}$ 2-heterolayer in the range of 80–250 nm, as reported in our previous studies [6].

A significant difference is also observed in the dielectric behavior of the 2-heterolayered PZT films as shown in Fig. 12. $PZ_{70}T_{30}$ 2-heterolayer has better dielectric properties with relative permittivity of 325 and dielectric loss of 0.03 than $PZ_{30}T_{70}$ 2-heterolayer with relative permittivity and dielectric loss of 221 and 0.04, respectively. Since both the films have been crystallized under the same heat treatment forming perovskite phase with (001)/(100) preferred orientation, the higher dielectric properties in $PZ_{70}T_{30}$ 2-heterolayer is caused by the significantly larger grain size of the film which facilitates domain wall movement. A detailed study on the effect of microstructure on the electrical properties of heterolayered PZT films has been reported in a separate paper [6].

The low permittivity observed for the 2-heterolayered film is due to the presence of an interfacial layer of low permittivity formed between the film and the top/bottom metal electrodes (electrode/film interfacial layers). In our previous studies, we compared the relative permittivity

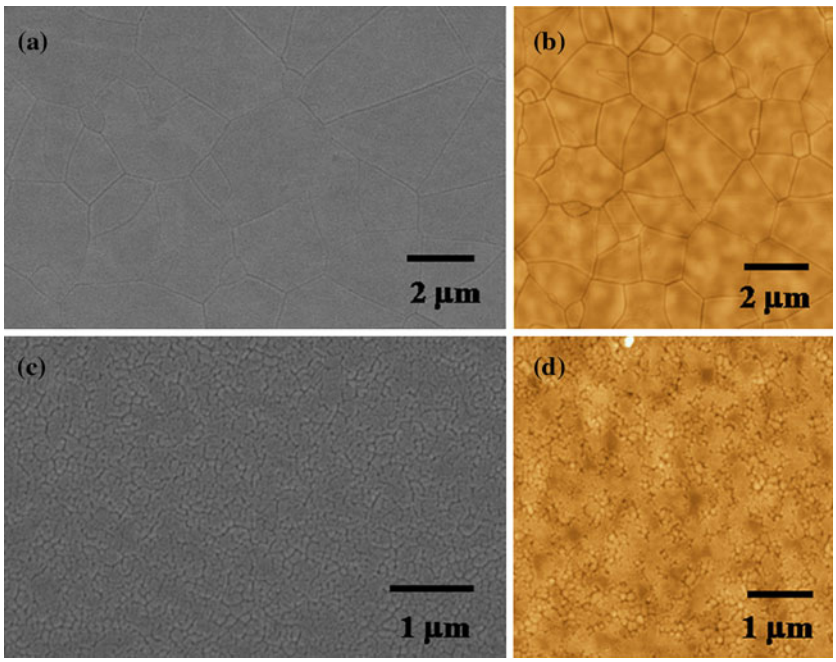

Fig. 11 SEM and AFM micrographs of **a**, **b** $PZ_{70}T_{30}$ 2-heterolayer and **c**, **d** $PZ_{30}T_{70}$ 2-heterolayer thin films

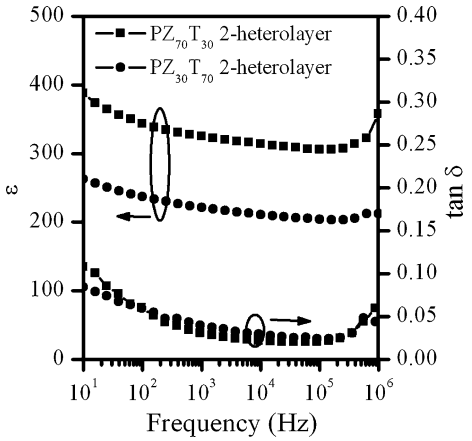

Fig. 12 Dielectric properties of $PZ_{70}T_{30}$ 2-heterolayer and $PZ_{30}T_{70}$ 2-heterolayer thin films

calculated on the basis of the capacitance series connection model with the experimentally measured values. It was concluded that the electrode/film interfacial layers had a dramatic effect in lowering the permittivity of thinner PZT films, which is the case for the 2-heterolayered PZT film. The relative permittivity of the heterolayered PZT film increases with increasing film thickness, and it approaches the theoretically calculated value, where a relatively smaller interfacial layer effect is expected [6, 32].

Effect of substrates

To confirm the minor effect played by the substrate on the microstructure for the heterolayered PZT thin films, heterolayered $PZ_{70}T_{30}$ films were deposited on other two different types of substrates, i.e., $SrRuO_3$/Pt(111)/Ti/SiO_2/Si(100) and $SrRuO_3/SrTiO_3$(100) (SRO/STO) with SRO thickness of ~50 nm. The SRO has s random orientation on both substrates. The textures of the heterolayered $PZ_{70}T_{30}$ films deposited on these substrates are shown in

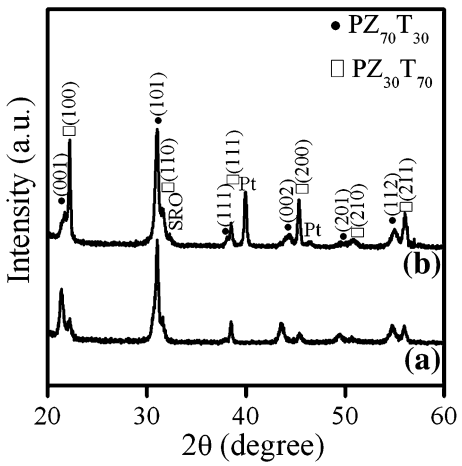

Fig. 13 XRD spectra of $PZ_{70}T_{30}$ 2-heterolayer on (*a*) SRO/STO and (*b*) SRO/Pt/Ti/SiO_2/Si substrates

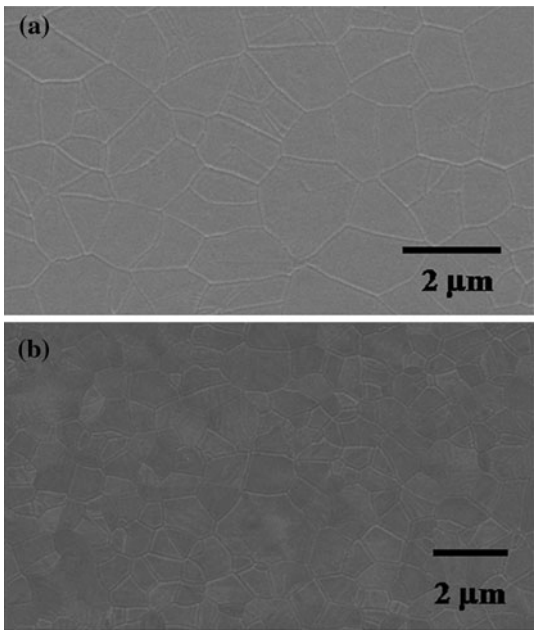

Fig. 14 SEM micrographs of $PZ_{70}T_{30}$ 2-heterolayer thin films on **a** SRO/Pt/Ti/SiO_2/Si and **b** SRO/STO substrates

Fig. 13. They are crystallized and exhibit a polycrystalline structure with random orientation. Figure 14 shows the SEM images of the $PZ_{70}T_{30}$ 2-heterolayer films deposited on SRO/Pt/Ti/SiO_2/Si and SRO/STO, respectively. The heterolayered PZT films apparently maintained the large grain sizes despite the usage of different substrates. The grain size of heterolayered PZT deposited on SRO/Pt/Ti/SiO_2/Si was in the range of 0.8–2.5 μm and the grain size of heterolayered PZT deposited on SRO/STO shows a similar grain size range. The observed little change in grain size of the heterolayered $PZ_{70}T_{30}$ films confirms that substrates have little significance in the formation of large grains in heterolayered $PZ_{70}T_{30}$ film.

Effect of thermal treatment

To look at the possible effect of thermal treatment on the microstructure development, the $PZ_{70}T_{30}$ layer of heterolayered $PZ_{70}T_{30}$ film was subjected to different thermal treatment. The first sample was prepared only by drying the $PZ_{70}T_{30}$ layer at 300 °C. For the second sample, the $PZ_{70}T_{30}$ layer underwent drying at 300 °C and then baking at 500 °C. For the third sample, the $PZ_{70}T_{30}$ layer underwent drying at 300 °C, baking at 500 °C, followed by further annealing at 650 °C. Each film sample was then spin-coated with $PZ_{30}T_{70}$ layer that was dried at 300 °C, baked at 500 °C, and finally annealed at 650 °C. From the SEM images, it is observed that the unusually large grain size can be obtained for heterolayered $PZ_{70}T_{30}$ films with amorphous and metastable fluorite phase with no

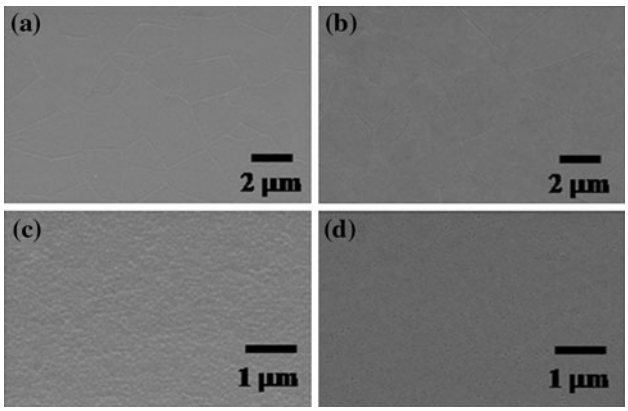

Fig. 15 SEM micrographs of $PZ_{70}T_{30}$ 2-heterolayer after annealing with $PZ_{70}T_{30}$ layer undergoing different thermal treatment **a** 300 °C, **b** 300 → 500 °C, **c** 300 → 500 → 650 °C, **d** $PZ_{30}T_{70}$ 2-heterolayer after annealing with $PZ_{30}T_{70}$ layer undergoing thermal treatment at 300 °C

well-defined grains $PZ_{70}T_{30}$ seeding layer as in the case of the first and second samples shown in Fig. 15a and b, respectively. When the crystallized perovskite structured $PZ_{70}T_{30}$ was used as the seeding layer, much smaller grains was observed for the heterolayered $PZ_{70}T_{30}$ film, as seen from Fig. 15c. Indeed, the top $PZ_{30}T_{70}$ layer was crystallized following the annealed single-layered $PZ_{70}T_{30}$ layer and the average grain size of the third sample was (160.6 ± 31.0) nm, which is similar to that of the two-layered $PZ_{70}T_{30}$ film (Fig. 6e). This confirms that in the third sample, the crystallized perovskite structured $PZ_{70}T_{30}$ provides a large number of nucleation sites for the top $PZ_{30}T_{70}$ and the overall film microstructure is dictated by the crystallized $PZ_{70}T_{30}$ seeding layer.

Further thermal treatment study was also done for the heterolayered $PZ_{30}T_{70}$ films, whereby a film with $PZ_{30}T_{70}$ seeding layer was heat treated only at 300 °C to form amorphous $PZ_{30}T_{70}$. After the heterolayered $PZ_{30}T_{70}$ was annealed at 650 °C, the overall film microstructure was refined as shown in Fig. 15d with an average grain size of (41.7 ± 7.5) nm, smaller than that of the heterolayered $PZ_{30}T_{70}$ with crystallized $PZ_{30}T_{70}$ layer baked at 500 °C. This suggests that by heating at lower temperature, in this case at 300 °C, the nuclei of $PZ_{30}T_{70}$ could not grow larger as in the case for $PZ_{30}T_{70}$ layer baked at higher temperature, causing the overall grain size to be smaller. Thus, the thermal treatment has rather different effect to the microstructure development of heterolayered $PZ_{70}T_{30}$ and $PZ_{30}T_{70}$ films.

Microstructure and texture development in heterolayered PZT films

It has been observed that by changing the stacking sequence, the microstructure of heterolayered PZT films can be changed significantly. The observation indicates that the microstructure development of the heterolayered PZT film is largely dependent on the choice of the first PZT layer which acts as the seeding layer. As has been mentioned briefly, the overall microstructure of the PZT film is closely related to the grain size of the seeding layer as it affects the kinetics of crystallization. Hence, in the seeded PZT film of heterolayered structure, the film microstructure can be controlled by choosing a seeding layer with desired grain size.

In the heterolayered $PZ_{70}T_{30}$ film, the unusual large grain size occurred for film thickness as thin as ~150 nm, regardless of the substrates used. It has been further observed that the large grain size can be formed upon baking at 500 °C, although the grain boundaries were not as well defined as that of the annealed heterolayered $PZ_{70}T_{30}$ film, as shown by the AFM images in Fig. 16. A significant change in the overall film texture is observed when the stacking sequence is changed, i.e., when $PZ_{30}T_{70}$ is employed as the seeding layer. In addition to the seeding layer effect, the heat treatment of the $PZ_{70}T_{30}$ seeding layer

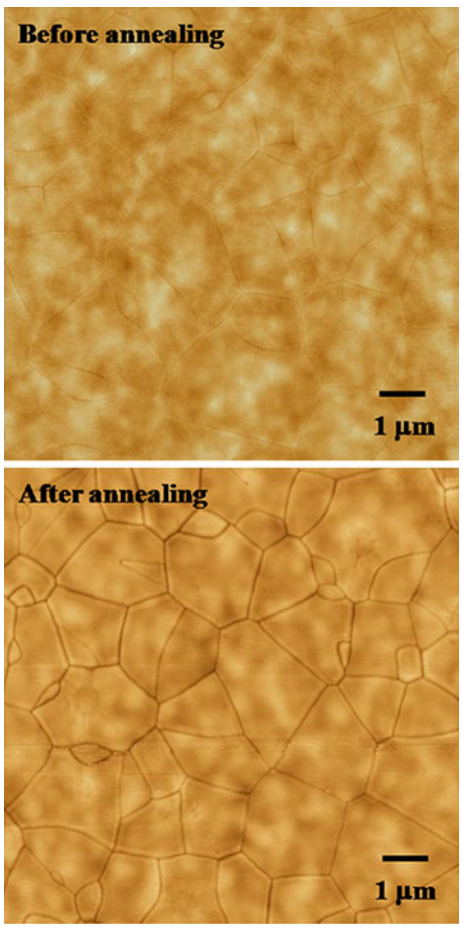

Fig. 16 AFM images of $PZ_{70}T_{30}$ 2-heterolayer before and after annealing at 650 °C

also plays an important role. The amorphous with no well-defined grains $PZ_{70}T_{30}$ seeding layer facilitates the development of large grains, which are not observed for the heterolayered $PZ_{70}T_{30}$ with a highly crystallized and well-defined grains $PZ_{70}T_{30}$ seeding layer.

It is then suggested that by stacking $PZ_{70}T_{30}$ and $PZ_{30}T_{70}$ together in the heterolayered $PZ_{70}T_{30}$ structure, the top $PZ_{30}T_{70}$ layer facilitates the crystallization of the $PZ_{70}T_{30}$ seeding layer during the baking process at 500 °C. This is apparently shown from the XRD traces of $PZ_{70}T_{30}$ 2-heterolayer film after baking shown in Fig. 9a, where the majority of the $PZ_{70}T_{30}$ 2-heterolayer had been crystallized into perovskite phase with a small amount of fluorite phase being present. The $PZ_{30}T_{70}$ layer promoted the nucleation of $PZ_{70}T_{30}$ seeding layer into perovskite phase by lowering the nucleation barrier such that the nucleation could occur at lower temperatures. The lower nucleation barrier could be explained by the similar lattice parameters between $PZ_{70}T_{30}$ ($a \sim 4.111$ Å) [49] and $PZ_{30}T_{70}$ ($a \sim 3.967$ Å and $c \sim 4.125$ Å) [50]. Previous studies have reported that a seeding layer could lower the nucleation activation energy in association with the lattice matching and thus, lower the transformation temperature to perovskite [51, 52]. In this study, it is the top $PZ_{30}T_{70}$ layer which facilitated the nucleation of the $PZ_{70}T_{30}$ seeding layer, as $PZ_{30}T_{70}$ exhibits lower nucleation energy than $PZ_{70}T_{30}$. As $PZ_{30}T_{70}$ with (100) preferred orientation promotes the crystallization of the $PZ_{70}T_{30}$ seeding layer, it also at the same time influences the texture of $PZ_{70}T_{30}$. With further thermal baking and annealing, the nuclei of $PZ_{70}T_{30}$ grew larger and dictated the microstructure development of the $PZ_{30}T_{70}$ layer, resulting in the unusually large grained film with high crystallinity, and at the same time maintaining the (001)/(100) preferred orientation, as shown schematically in Fig. 17.

In the heterolayered $PZ_{30}T_{70}$ films, the $PZ_{30}T_{70}$ seeding layer which exhibits a low nucleation energy, could form

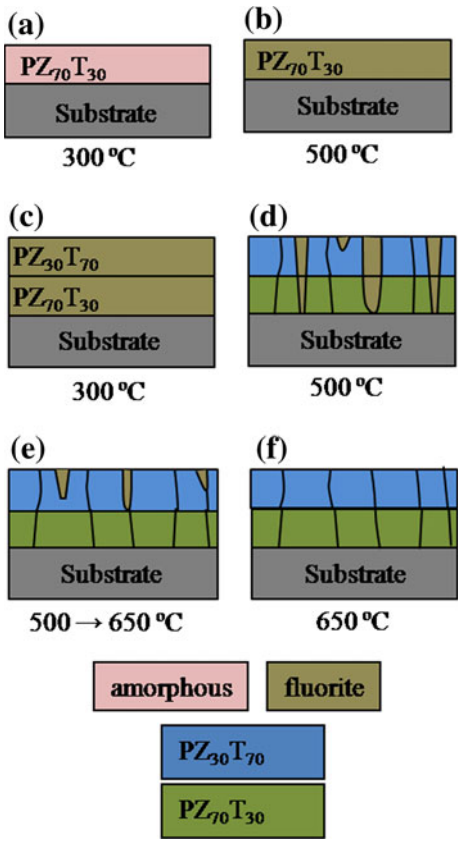

Fig. 17 Schematic diagram for microstructure development of $PZ_{70}T_{30}$ 2-heterolayer. **a** The $PZ_{70}T_{30}$ layer is dried at 300 °C forming amorphous phase, followed by **b** baking at 500 °C forming the fluorite phase. **c** The $PZ_{30}T_{70}$ was deposited and dried at 300 °C, followed by **d** baking at 500 °C whereby it promoted the crystallization of the $PZ_{70}T_{30}$ seeding layer, **e**, **f** with further baking and annealing processes the film became fully crystallized and the grains became larger resulting in the unusually large grained heterolayered film

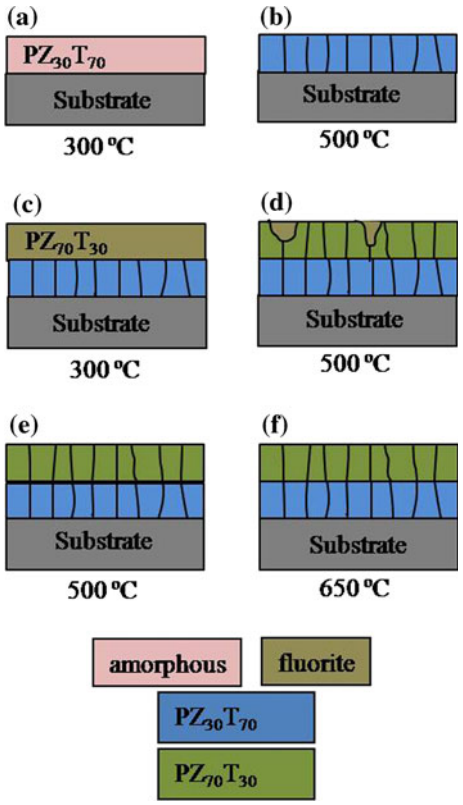

Fig. 18 Schematic diagram for microstructure development in $PZ_{30}T_{70}$ 2-heterolayer. **a** The $PZ_{30}T_{70}$ layer is dried at 300 °C forming amorphous phase, followed by **b** baking at 500 °C forming crystallized perovskite phase. **c** The $PZ_{70}T_{30}$ was deposited and dried at 300 °C, followed by **d**, **e** baking at 500 °C whereby it crystallized following the microstructure of $PZ_{30}T_{70}$. **f** The heterolayered $PZ_{30}T_{70}$ was annealed at 650 °C forming fully crystallized film with small microstructure

more nuclei and eventually crystallized forming small grains with (100) preferred orientation as the film is baked at 500 °C. These crystallized grains provided nucleation sites for the top $PZ_{70}T_{30}$ and the overall texture of heterolayered $PZ_{30}T_{70}$ followed that of $PZ_{30}T_{70}$ layer, resulting in fine grain sizes in the range of 80–250 nm with (001)/(100) preferred orientation. The proposed texture development of heterolayered $PZ_{30}T_{70}$ film is shown in Fig. 18.

Conclusions

Single-layered $PZ_{70}T_{30}$ thin film exhibits a higher crystallization temperature than that of the single-layered $PZ_{30}T_{70}$ film, as shown by both XRD phase analysis and Raman studies. While $PZ_{30}T_{70}$ could crystallize at 500 °C with (100) preferred orientation, $PZ_{70}T_{30}$ could only be crystallized to perovskite phase upon thermal annealing at 650 °C with random texture. The (100) preferred orientation in the single-layered $PZ_{30}T_{70}$ can be accounted for by the formation of PbO(100) seeding layer due to the oxidation of Pt_xPb phase at the intermediate pyrolysis temperature. The random film texture of the single-layered $PZ_{70}T_{30}$ is related to the volatility of PbO, giving rise to a large number of random nuclei to form and grow. The highly volatility of Pb in PZT was revealed by XPS study whereby the intensity of Pb peaks of single-layered $PZ_{70}T_{30}$ was lower than that of single-layered $PZ_{30}T_{70}$. When the film thickness is thin ($\sim$75 nm), the two single-layered films show similar film microstructures. However, with increasing film thickness, $PZ_{70}T_{30}$ grew into much larger grain sizes as compared to $PZ_{30}T_{70}$, accompanied by the formation of a rosette structure due to the Pb volatility. An unusually large grain size in the range of 1–3 μm has been observed for the heterolayered $PZ_{70}T_{30}$ film for film thickness as thin as $\sim$150 nm. The unusually large grain sizes were identified as arising from the $PZ_{70}T_{30}$ seeding layer, the phases present in which are largely dictated by the thermal treatment temperature. The coarse-grained film is developed when the $PZ_{70}T_{30}$ seeding layer is retained at amorphous or fluorite phase with no well-defined grains, rather than in a crystallized perovskite phase. In the heterolayered $PZ_{70}T_{30}$ film, the $PZ_{30}T_{70}$ layer lowers the nucleation barrier of $PZ_{70}T_{30}$ layer, causing it to crystallize to perovskite phase at lower temperature following the texture of $PZ_{30}T_{70}$ layer. This gives rise to the formation of large-grained film with (001)/(100) preferred orientation upon further annealing at 650 °C. When $PZ_{30}T_{70}$ layer acts as the seeding layer, the heterolayered film is developed into an overall, refined grain structure with (001)/(100) preferred orientation as the top $PZ_{70}T_{30}$ layer nucleates following the small grain-sized $PZ_{30}T_{70}$ seeding layer with (100) preferred orientation.

Acknowledgements This paper is based upon work supported by the Science and Engineering Research Council–A*Star, Singapore. Research at UNSW was supported by an Australian Research Council Discovery Project and UNSW Anthony Mason travel grant. The authors would like to thank Dr. Debbie Seng Hwee Leng, Mr. Tan Chee King, and Dr. Gregory Goh for their time and efforts on SIMS measurements, Ms. June Ong Lay Ting for her assistance in XPS measurements, and Dr. X. J. Lou for his time in discussion. The authors would like to acknowledge the support of National University of Singapore in this project.

References

1. Brooks KG, Reaney IM, Klissurska R, Huang Y, Bursil L, Setter N (1994) J Mater Res 9:2540
2. Cheng J, Meng Z (2000) J Mater Sci Lett 19:1945
3. Kwok CK, Desu SB (1993) J Mater Res 8:339
4. Spierings GAMC, Zon JBAv, Klee M, Larsen PK (1993) Integr Ferroelectr 3:283
5. Zhang S, Liu J, Yang C (2006) Integr Ferroelectr 84:99
6. Kartawidjaja FC, Sim CH, Wang J (2009) J Mater Sci 44:5375. doi:10.1007/s10853-009-3569-6
7. Yan F, Bao P, Chan LW, Choy CL, Wang Y (2002) Thin Solid Films 406:282
8. Hirano S, Yugo T, Kikuta K, Araki Y, Saitoh M, Ogasahara S (1992) J Am Ceram Soc 75:2785
9. Hwang KS, Manabe T, Nagahama T, Yamaguchi I, Kumagai T, Mizuta S (1999) Thin Solid Films 347:106
10. Wood VE, Busch JR, Ramamurthi SD, Swartz SL (1992) J Appl Phys 71:4557
11. Choi JJ, Park CS, Park GT, Kima HE (2004) Appl Phys Lett 85:4621
12. Choi JJ, Park GT, Park CS, Lee JW, Kim HE (2004) J Mater Res 19:3671
13. Doi H, Atsuki T, Soyama N, Sasaki G, Yonezawa T, Ogi K (1994) Jpn J Appl Phys Part 1 3:5159
14. Chen SY, Chen IW (1998) J Am Ceram Soc 81:97
15. Gong W, Li JF, Chu X, Li L (2004) J Eur Ceram Soc 24:2977
16. Reaney IM, Brooks KG, Klissurska R, Pawlaczyk C, Setter N (1994) J Am Ceram Soc 77:1209
17. Aoki K, Fukuda Y, Nishimura A (1993) Jpn J Appl Phys Part 1 32:4147
18. Hahn BD, Park DS, Choi JJ, Yoon WH, Ryu J, Kim DY (2008) J Mater Res 23:226
19. Kumar CVRV, Pascual R, Sayer M (1992) J Appl Phys 71:864
20. Lee JS, Joo SK (2002) J Appl Phys 92:2658
21. Liu Y, Phule PP (1996) J Am Ceram Soc 79:495
22. Chen SY, Chen IW (1994) J Am Ceram Soc 77:2332
23. Schneller T, Kohlstedt H, Petraru A, Waser R, Guo J, Denlinger J, Learmonth T, Glans P-A, Smith KE (2008) J Sol-Gel Sci Technol 48:239
24. Schneller T, Waser R (2007) J Sol-Gel Sci Technol 42:337
25. Huang Z, Zhang Q, Whatmore RW (1998) J Mater Sci Lett 14:1157
26. Wu A, Vilarinho PM, Reaney I, Salvado IMM (2003) Chem Mater 15:1147
27. Chen SY, Chen IW (1994) J Am Ceram Soc 77:2337
28. Polli AD, Lange FF, Levi CG (2000) J Am Ceram Soc 83:873
29. Subramanian MA, Aravamudan G, Rao GVS (1983) Prog Solid State Chem 15:55

30. Muralt P (2006) J Appl Phys 100:051605-1
31. Schwartz RW (1997) Chem Mater 9:2325
32. Kartawidjaja FC, Sim CH, Wang J (2007) J Appl Phys 102:124102-1
33. Kartawidjaja FC, Zhou ZH, Wang J (2006) J Electroceram 16:425
34. Anbusathaiah V, Kan D, Kartawidjaja FC, Mahjoub RM, Arredondo MA, Wicks S, Takeuchi I, Wang J, Nagarajan V (2009) Adv Mater 21:3497
35. Wilkinson AP, Speck JS, Cheetham AK (1994) Chem Mater 6:750
36. Genechten DV, Vanhoyland G, Haen JD, Johnson J, Wouters DJ, Bael MKV, Rul HVd, Poucke LCV (2004) Thin Solid Films 467:104
37. Thomas R, Mochizuki S, Mihara T, Ishida T (2001) Jpn J Appl Phys Part 1 40:5511
38. Atsuki T, Soyama N, Sasaki G, Yonezawa T, Ogi K, Sameshima K, Hoshiba K, Nakao Y, Kamisawa A (1994) Jpn J Appl Phys Part 1 33:5196
39. Taguchi I, Pignolet A, Wang L, Proctor M, Levy F, Schmid PE (1993) J Appl Phys 74:6625
40. Yi H, Kim MG, Park J, Jang HM (2004) J Appl Phys 96:5110
41. Meng JF, Katiyar RS, Zou GT, Wang XH (1997) Phys Stat Sol (a) 164:851
42. Burns G, Scott BA (1970) Phys Rev Lett 25:1191
43. Agrawal DC, Majumder SB, Mohapatra YN, Sathaiah S, Bist HD, Katiyar RS, Prado EC, Reynes A (1993) J Raman Spectrosc 24:459
44. Zhang H, Leppavuori S, Karjalainen P (1995) J Appl Phys 77:2691
45. Park CS, Lee JW, Park GT, Kim HE, Choi JJ (2007) J Mater Res 22:1367
46. Sugiyama O, Kondo Y, Suzuki H, Kaneko S (2003) J Sol-Gel Sci Technol 26:749
47. Wakiya N, Kuroyanagi K, Xuan Y, Shinozaki K, Mizutani N (2000) Thin Solid Films 372:156
48. Zhu TJ, Lu L (2004) J Appl Phys 95:241
49. Khaenamkaew P, Muensit S, Bdikin IK, Kholkin AL (2007) Mater Chem Phys 102:159
50. Escote MT, Pontes FM, Leite ER, Longo E, Jardim RF, Pizani PZ (2004) J Appl Phys 96:2186
51. Huang Z, Zhang Q, Whatmore RW (1999) J Appl Phys 85:7355
52. Wu A, Vilarinho PM, Reaney IM, Salvado IMM, Baptista JL (2000) Integr Ferroelectr 31:261